

Enhancing Irradiation Resistance in Refractory Medium Entropy Alloys with Simplified Chemistry

M.A. Tunes^{a,*}, D. Parkison^{b,c}, B. Sun^d, P. Willenshofer^a, S. Samberger^a, B.K. Derby^e, J.K.S. Baldwin^e, S.J. Fensin^e, D. Sobieraj^f, J.S. Wróbel^f, J. Byggmästar^g, S. Pogatscher^a, E. Martinez^d, D. Nguyen-Manh^{h,i}, O. El-Atwani^j

^aChair of Non-Ferrous Metallurgy, Montanuniversität Leoben, Austria

^bMaterials Science and Technology Division, Los Alamos National Laboratory, United States

^cDepartment of Nuclear Engineering, University of California at Berkeley, United States

^dDepartments of Mechanical Engineering and Materials Science and Engineering, Clemson University, United States

^eCenter for Integrated Nanotechnologies, Los Alamos National Laboratory, United States

^fFaculty of Materials Science and Engineering, Warsaw University of Technology, Poland

^gDepartment of Physics, University of Helsinki, Finland

^hMaterials Division, United Kingdom Atomic Energy Authority, Culham Campus, Abingdon, United Kingdom

ⁱDepartment of Materials, University of Oxford, Parks Road, United Kingdom

^jReactor Materials and Mechanical Design, Pacific Northwest National Laboratory, United States

Abstract

Refractory High-Entropy Alloys (RHEAs) hold promising potential to be used as structural materials in future nuclear fusion reactors, where W and its alloys are currently leading candidates. Fusion materials must be able to withstand extreme conditions [1, 2], such as (i) severe radiation-damage arising from highly-energetic neutrons, (ii) embrittlement caused by implantation of H and He ions, and (iii) exposure to extreme high-temperatures and thermal gradients. Recent research demonstrated that two RHEAs – the WTaCrV [3] and WTaCrVHf [4] – can outperform both coarse-grained and nanocrystalline W in terms of its radiation response and microstructural stability [5–8]. Chemical complexity and nanocrystallinity enhance the radiation tolerance of these new RHEAs, but their multi-element nature, including low-melting Cr, complicates bulk fabrication and limits practical applications. Herein, we demonstrate that reducing the number of alloying elements and yet retain high-radiation tolerance is possible within the ternary system W–Ta–V via synthesis of two novel nanocrystalline refractory medium-entropy alloys (RMEAs): the $W_{53}Ta_{44}V_3$ and $W_{53}Ta_{42}V_5$ (in at.%). We experimentally show that the radiation response of the W–Ta–V system can be tailored by small additions of V, and such experimental result was validated with theoretical analysis of chemical short-range orders (CSRO) from combined ab-initio atomistic Monte-Carlo modeling. It is predicted from computational analysis that a small change in V concentration has a significant effect on the Ta-V CSRO between $W_{53}Ta_{44}V_3$ and $W_{53}Ta_{42}V_5$ leading to radiation-resistant microstructures in these RMEAs from chemistry stand-point of views. By returning to terminal solid solutions, we deviate from the original high-entropy alloy concept to show that high radiation resistance can be achieved in systems with simplified chemical complexity, hinting at a new paradigm for the metallurgy of high-entropy and highly-concentrated multi-component alloys.

Keywords: Refractory Medium Entropy Alloys, Fusion Materials, Radiation Damage, High Entropy Alloys, *In situ* TEM

*Corresponding authors:

Email address: matheus.tunes@unileoben.ac.at (M.A. Tunes)

1. Introduction

Since the 1970s, materials selection for application in future thermonuclear fusion reactors has posed a significant challenge for materials science and metallurgy [2, 9–13]. The deuterium-tritium fusion reaction exposes fusion reactors and their structural materials to exceptionally harsh environmental conditions. To date, considering the design and selection of materials for experimental fusion reactors, the following key factors must be addressed, not exhaustively [2, 9–13]:

- Impact of highly mono-energetic fusion neutrons (14.1 MeV) resulting in radiation damage;
- Implantation of helium (He) and hydrogen (H) ions at moderate-to-low energies after thermalization in the plasma, resulting in synergistic radiation damage, inert gas bubbles nucleation and growth and materials embrittlement; and
- The presence of a plasma with high-power density, resulting in high-temperature exposure in thermal gradients.

As the 21st century began, two critical objectives arose that must be addressed to render fusion reactors feasible: (i) better controlling the high-power plasma with (ii) concomitant enhancement of its performance [2]. For these reasons, materials science has redirected its attention towards better understanding plasma-materials interactions [14]. The surface of plasma-facing materials will be constantly subjected to the severe degradation forces aforementioned, which can significantly hinder the fusion reactor operation [2]. Currently, beryllium (Be) [2, 15] and tungsten (W) [2] are being considered for use in the first-wall armor, while W is the choice for divertor applications [16–21].

A significant challenge associated with the potential use of W in fusion reactors was highlighted in a 1998 article by Davis *et al.* [16], which assessed W for application in the International Thermonuclear Experimental Reactor (ITER). The conclusion of this assessment stated that W was not suitable for use in ITER due to its low strength, limited thermal shock resistance, and high ductile-brittle transition temperature (DBTT) [16]. Moreover, beyond the issues of low strength and brittleness, studies on energetic particle irradiation response have revealed a series of irradiation effects and microstructural changes in W that cannot be ignored [22–24]. These irradiation effects, when emulated with particle accelerators – as recently reviewed and summarized by Harrison [24] – include a high density of dislocation loops and the formation of He bubbles [25, 26], both of which can further increase W brittleness through irradiation-induced hardening. Ferroni *et al.* also reported that when radiation damage is formed in W, even high temperature isochronal annealing is not able to fully recover defects in the W microstructure [27].

The challenge associated with improving mechanical properties of W has attracted increased attention of the greater materials and metallurgical engineering communities in the recent years [21, 28]. Various approaches have been explored, including reducing the grain size of W through methods such as cold-rolling [28–31], wire drawing [32–35], and severe-plastic deformation (SPD) [36, 37]. Another avenue involves grain-boundary doping [21, 38–40], although challenges associated with intragranular fracture and fracture resistance of nanocrystalline W are still pending resolution and can be considered topics for further research [41–44]. Nevertheless, it is worth noting that recent radiation damage studies

– carried out with light- and heavy-ion irradiation within *in situ* transmission electron microscopy (TEM) independently at both the IVEM facility in USA [45] and the MIAMI facility in UK [46, 47] – have shown that even nanocrystalline W experience severe damage from energetic particle irradiation [5–8], thus raising questions regarding the overall feasibility of proposing W for fusion applications. It is important emphasizing that *in situ* TEM ion irradiation studies on coarse-grained W and select W-alloys also indicated extensive formation of radiation damage defects in a similar manner [48–50]. Neither an irradiation nor thermal stability study have yet been conducted on doped nanocrystalline W, indicating potential for future research still considering this element a candidate as fusion material.

An alternative to W in fusion applications is presented by the field of high-entropy alloys (HEAs) [51–55], and more specifically due to their high-temperature resilience, the refractory high-entropy alloys (RHEAs) [56–59]. Composed of four or more alloying elements in near-equimolar concentrations, these alloys are designed to maximize configurational entropy and minimize Gibbs free energy, thereby enhancing thermodynamic stability of the solid solution phase. Nanocrystalline RHEAs can be fabricated by several methods [60], including both SPD [61, 62] and mechanical alloying [63] for macro-scale samples, and magnetron-sputtering [64, 65] for nano-scale prototypic samples: the latter aiming at fast irradiation screening. It is important to emphasize that not all nanocrystalline HEAs and RHEAs can be considered radiation-tolerant for fusion applications [66–68] and detailed studies should be carried out for each specific alloy under consideration.

Recently, two particular RHEAs systems have attracted the attention of the fusion materials community: the W–Ta–Cr–V [3, 68] and the W–Ta–Cr–V–Hf [4, 68]. In the first quaternary system, the $W_{38}Ta_{36}Cr_{15}V_{11}$ RHEA (in at.%), demonstrated superior radiation resistance compared to nanocrystalline W [5–8], particularly in mitigating displacement damage formation such as dislocation loops, yielding negligible irradiation hardening assessed via nanomechanical testing. On the downside, this $W_{38}Ta_{36}Cr_{15}V_{11}$ RHEA experienced radiation-induced precipitation (RIP), characterized by the formation of Cr-V rich precipitates at a radiation dose of 8 dpa (displacement-per-atoms). In the second system, irradiation testing on the nanocrystalline RHEA – the $W_{29}Ta_{42}Cr_5V_{16}Hf_8$ (in at.%) revealed that neither dislocation loops nor precipitates have formed after a dose of 10 dpa [4]. Although such recent studies on these two RHEAs show that increased chemical complexity enhances radiation resistance and stability in harsh environments [3, 4, 68], increasing the number of alloying elements in any RHEA system complicates their bulk fabrication, crucial for practical engineering applications: for example, the low-melting point of Cr impairs the feasibility for the fabrication of both $W_{38}Ta_{36}Cr_{15}V_{11}$ and $W_{29}Ta_{42}Cr_5V_{16}Hf_8$ RHEAs. Therefore, a key question arises: can the number of alloying elements be reduced in these RHEA systems without compromising their high radiation resistance?

In this study, we show that it is feasible to simplify the quinary RHEA system, the W–Ta–Cr–V–Hf, to a ternary refractory medium-entropy alloy (RMEA) system, the W–Ta–V, resulting in the development of a novel nanocrystalline RMEA, the $W_{53}Ta_{42}V_5$ (in at.%). A recent computational study indicated the WTaV system as a potential and most-promising low-activation RMEA with superior radiation resistance when compared with recent RHEAs proposed for application in irradiation environments [69]. We demonstrate that the new ternary RMEA not only retains the irradiation resistance observed previously for more complex RHEAs [3, 4, 68], but also surpasses the irradiation resistance of the binary ultrafine-grain (UFG)

$W_{44}Ta_{56}$ (in at.%) highly-concentrated refractory alloy. Through detailed post-irradiation analysis and atomistic Monte-Carlo (MC) simulations, we investigate the underlying mechanisms of irradiation resistance in this new ternary system, focusing on the role of minor V additions to the irradiation resistance output. We show both theoretically and experimentally that small additions of V drastically changes the non-irradiation resistant binary WTa system by forming a new irradiation resistant alloy – the nanocrystalline ternary WTaV RHEA. In addition, we show demonstrate for the first time that the element Cr is not needed for RHEAs in the context of fusion applications, opening an unprecedented pathway for the synthesis of these novel metallic alloys in bulk and large-scale quantities.

2. Results and Discussion

2.1. Morphological stability under extreme conditions

Heavy ion irradiation with *in situ* TEM allowed for the comparison of two different RMEAs within the ternary system W-Ta-V, the $W_{53}Ta_{42}V_5$ and the $W_{53}Ta_{44}V_3$. It is important emphasizing that the major objective of the study was to identify the role of the element V in these two alloys' response to both high-temperature annealing (maximum temperature was 1173 K) and high-dose irradiation at high-temperatures (maximum average dose was 20 dpa at an irradiation temperature of 1073 K).

Bright-Field TEM (BFTEM) micrographs of the $W_{53}Ta_{44}V_3$ and the $W_{53}Ta_{42}V_5$ recorded at three different conditions – pristine, after annealing at 1173 K, and after irradiation at 1073 K – are shown in Fig. 1. Before both irradiation and annealing (Fig. 1A and 1D), these alloys exhibited equiaxed grains within the nanocrystalline regime (*i.e.*, <100 nm). Apart from the chemical composition, no major differences between these two RMEAs were detected or identified. By analysing the BFTEM micrographs after annealing (Fig. 1B and 1E) and irradiation (Fig. 1C and 1F), it was noticeable that the $W_{53}Ta_{44}V_3$ RMEA experienced a modest grain growth, particularly noted after 20 dpa of irradiation. Conversely, the $W_{53}Ta_{42}V_5$ RMEA was seemingly unaltered after both annealing and irradiation. A quantitative analysis of average grain sizes as a function of the conditions studied in this work is shown in Table 1.

These results exhibited in Fig. 1 are better comprehended considering the challenges on the application of nanocrystalline alloys in extreme environments. These challenges are intrinsically related with the (thermodynamic and morphological) stability of nanocrystalline materials [70–72] when subjected to exposure in both irradiation [73] and high-temperatures [74]. In this context, the primary adverse consequence of such exposure is grain growth as numerous material properties stem from the average grain size. To date, and according to Zhang *et al.* [73], a limited number of studies addressed the grain size stability of nanocrystalline metallic alloys, and in this way, existing studies on this field are primarily focused on the behaviour of nanocrystalline elemental metals. Herein, it is consolidated that elemental metals in their nanocrystalline form experience significant grain growth under heating/annealing and accelerated grain growth under irradiation over a wide range of temperatures. With respect to nanocrystalline elemental metals exposed to extreme conditions, it is important to emphasize that theoretical models were already developed and experimentally validated to explain such observations [75–78].

Nanocrystallinity allows achieving higher radiation tolerance within the scope of novel nuclear materials [6, 79–81]. This is due to the presence of a greater number of interfaces (namely grain boundaries)

that enhances the capacity for radiation-induced crystalline defects to be absorbed and recombine effectively at these site-specific dependencies [79, 80]. This is historically known and defined as "sink efficiency", and for a metal, the sink efficiency increases exponentially with decreasing average grain size [79, 80]. When nanocrystalline alloys undergo grain growth or recrystallization due to energetic particle irradiation, their radiation tolerance is compromised. In such cases, the challenges that affect W for fusion reactors [5–8, 22–24] also become relevant for both RHEAs and novel RMEAs. Concerning the current state of research on RHEAs, which are undergoing intensive development for fusion applications, it is worth noting that although there are limited studies on grain size stability under irradiation and high-temperature conditions, recent research reveals two critical findings: (i) not all nanocrystalline HEAs exhibit irradiation tolerance [66, 67], and (ii) certain RHEAs demonstrate superior performance

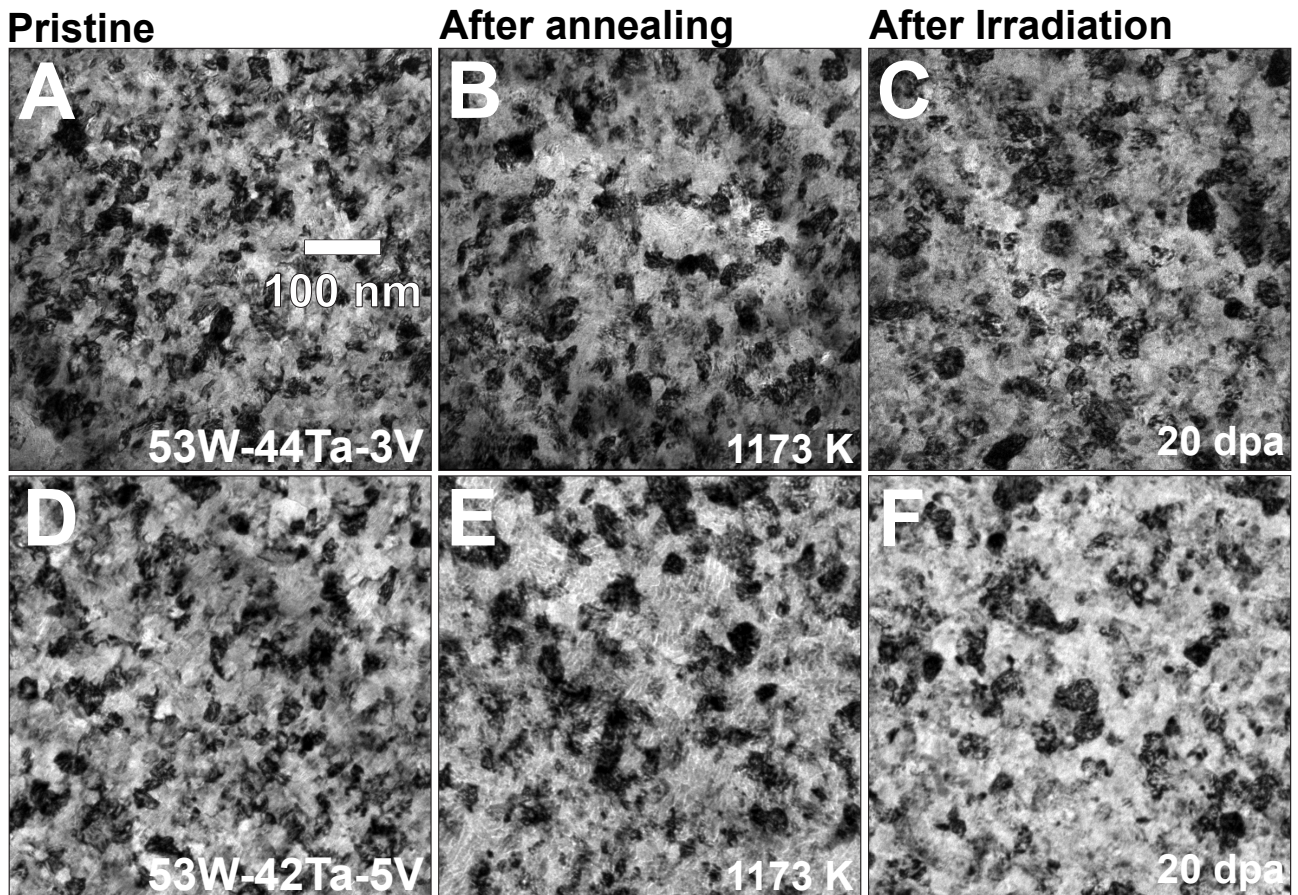


Figure 1: **Microstructural response to annealing and irradiation** | BFTEM micrographs taken at pristine condition, after annealing (at 1173 K) and after irradiation (at 1073 K) are shown in **A-C** and **D-F**, respectively for the $W_{53}Ta_{44}V_3$ and the $W_{53}Ta_{42}V_5$ RMEAs.

Table 1: Average grain size of RMEAs at pristine, after annealing and irradiation conditions.

Alloy Condition	Average Grain Size [nm]	
	53W-42Ta-3V [at.%]	53W-44Ta-5V [at.%]
Pristine (0 dpa)	19.2±0.9	25.9±1.0
Annealed at 1173 K (0 dpa)	27.5±0.9	29.1±1.4
Irradiated at 1073 K (20 dpa)	29.4±1.3	27.3±2.1

under irradiation at high-temperatures than both coarse-grained and nanocrystalline W [3–8, 82].

Precipitation was observed in the quaternary nanocrystalline RHEA – $W_{38}Ta_{36}Cr_{15}V_{11}$ [3] – when tested under heavy-ion irradiation, and although no significant alterations in the grain morphology were observed, such phase evolution effects are signs of degradation of the initially designed alloy. A new quinary RHEA [4] – $W_{29}Ta_{42}Cr_5V_{16}Hf_8$ [4] – was recently designed and synthesized. In terms of grain morphology after irradiation, the addition of Hf was associated with grain refinement/fragmentation during both annealing and irradiation, therefore indicating some grain instabilities that deserve further investigations. Although these previous works indicated that higher phase stability was achieved by increasing the chemical complexity, morphological changes were still observed in the microstructures of both alloys after irradiation. In comparison with both the $W_{38}Ta_{36}Cr_{15}V_{11}$ [3] and the $W_{29}Ta_{42}Cr_5V_{16}Hf_8$ [4] RHEAs, the results presented in Fig. 1 show that new RMEAs with lower chemical complexity – $W_{53}Ta_{42}V_5$ and the $W_{53}Ta_{44}V_3$ – can be synthesized in its nanocrystalline form and still preserve high microstructural stability after both high-temperature annealing and irradiation exposure observed in the RHEAs with more alloying elements. The average grain sizes measured at pristine, after annealing at 1173 K and after irradiation at 1073 K and up to 20 dpa attests these findings. These results presented in Table 1 suggest that high-temperature annealing drives grain growth due to the removal of voided grain boundaries manifested as nanoporosity in the pristine samples after magnetron-sputtering deposition [83]: evidence for such nanoporosity is presented in the supplemental information file. Conversely, irradiation at 1073 K after annealing indicates no detectable grain growth up to the tested dose of 20 dpa. Therefore, we can conclude that both W–Ta–V RMEAs exhibit a high degree of irradiation tolerance in terms of grain stability, as evidenced by the absence of growth and/or recrystallization after high-dose irradiation.

The phase stability of both W–Ta–V RMEAs was also investigated with the SAED technique during the *in situ* TEM experiments of high-temperature annealing and heavy-ion irradiation. Figs. 2A and 2D show the SAED patterns collected on the two different W–Ta–V RMEAs in their pristine condition; both alloys were indexed to have BCC crystalline structure matching W standards [84, 86]. The phase of both alloys remained unaltered after high-temperature annealing, as noted in Figs. 2B and 2E. After irradiation up to 20 dpa, some additional Debye-Scherrer rings appeared in the SAED patterns of both alloys, as shown in Figs. 2C and 2F, although in the alloy with higher V content (Fig. 2C), these rings are of lower intensity. These extra-rings could not be identified to any specific crystal structure or symmetry. It is important to emphasize that recently, these extra rings were also observed in the quinary $W_{29}Ta_{42}Cr_5V_{16}Hf_8$ RHEA after irradiation and as such, they were not indexed to any known phase [4].

The microstructure of both W–Ta–V alloys, as depicted in Fig. 1, reveals no phase transformation following high-temperature annealing or irradiation. The appearance of additional rings in the SAED patterns, as shown in Fig. 2, after a dose of 20 dpa, suggests the potential occurrence of phase instabilities through precipitation, thus underscoring the need for further nanoscale post-irradiation screening with analytical microscopy methods.

2.2. Chemical stability under extreme conditions

Scanning Transmission Electron Microscopy coupled with Energy Dispersive X-ray (STEM-EDX) spectroscopy mapping was performed to assess the local chemistry of both W–Ta–V RMEAs after heavy-ion

irradiation at 1173 K up to 20 dpa. Figs. 3A and 3B show the microstructure of the irradiated $W_{53}Ta_{42}V_5$ and the $W_{53}Ta_{44}V_3$ RMEAs, respectively, using both high-angle annular dark-field (HAADF) and EDX elemental maps. While the $W_{53}Ta_{44}V_3$ RMEA clearly indicates the occurrence of W segregation and Ta depletion at grain boundaries, no such segregation was observed or detected in the $W_{53}Ta_{42}V_5$ RMEA. Complimentary STEM-EDX maps for both pristine and annealed-only conditions are shown in the supplemental information file.

The nanoscale analytical assessment presented in Fig. 3 for both alloys after irradiation suggests that lower concentrations of V reduce the chemical stability of the W–Ta–V system. Interestingly, the $W_{53}Ta_{42}V_5$ RMEA not only exhibit high morphological stability under irradiation (Fig. 2), preventing grain growth or recrystallization up to a dose of 20 dpa at 1073 K, but also presents high chemical stability given the absence of grain boundary segregation under the irradiation conditions studied. These results shed light on the behavior that these RMEAs – manifested by the reduction on the number of alloying elements when compared with conventional RHEAs [3, 4] – can have their radiation response tailored as a function of the concentration of V. Therefore, further investigation is needed to explore the specific role of V in the context of the W–Ta–V system.

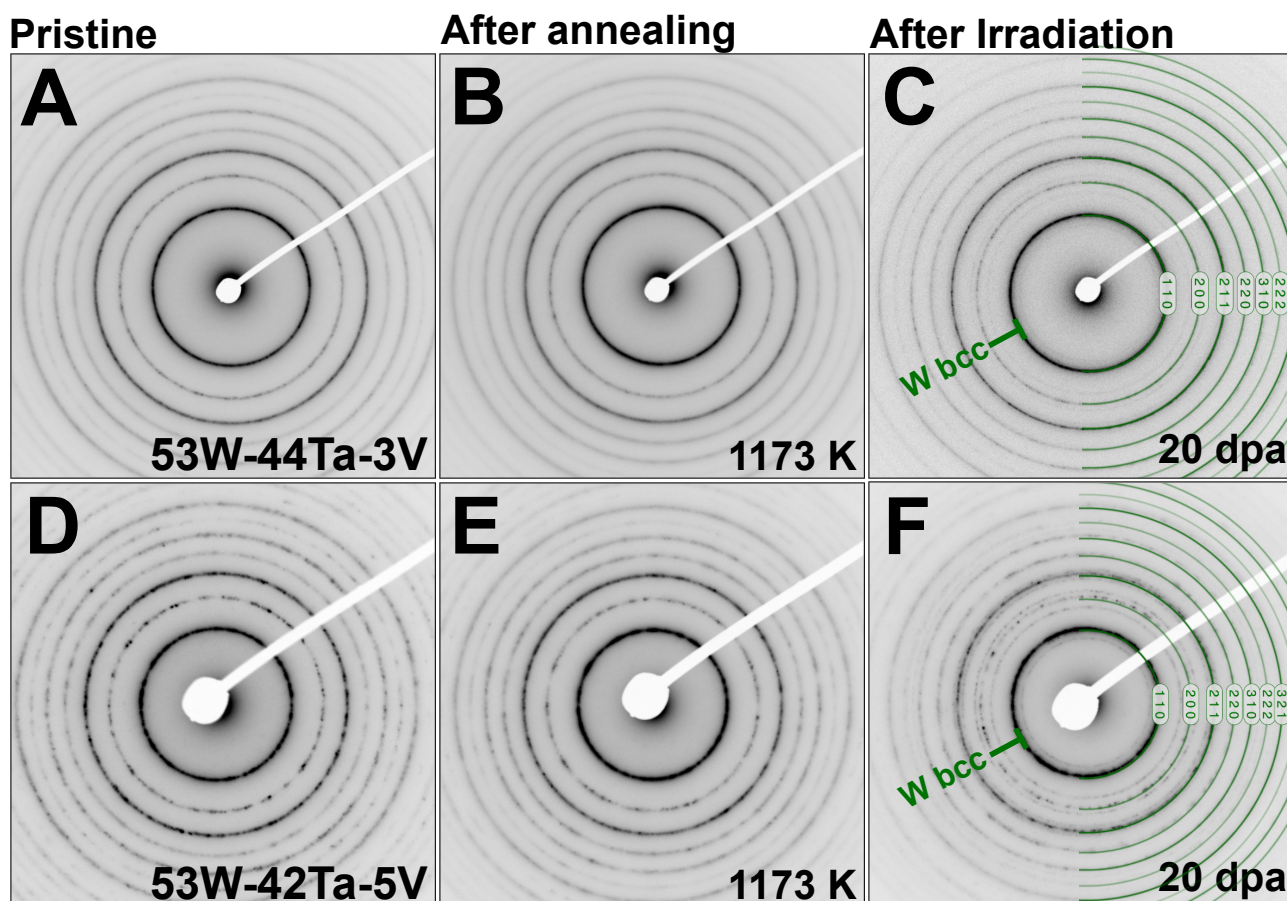


Figure 2: **Phase stability to annealing and irradiation** | SAED patterns collected at pristine condition, after annealing (at 1173 K) and after irradiation (at 1073 K) are shown in **A-C** and **D-F**, respectively for $W_{53}Ta_{44}V_3$ and the $W_{53}Ta_{42}V_5$ RMEAs. Additional rings were noted following irradiation, with a higher intensity observed in the $W_{53}Ta_{42}V_5$ RMEA (in **F**) compared to the $W_{53}Ta_{44}V_3$ RMEA (in **C**). Indexing was performed with data available in literature [84–87].

2.3. The role of V in the stability and radiation response of chemically simplified RMEAs

To investigate the role of V on the radiation response of the W–Ta–V system, additional high-temperature irradiation experiments were conducted using a binary UFG $W_{44}Ta_{56}$ alloy synthesized under similar deposition conditions. The microstructure of the UFG $W_{44}Ta_{56}$ alloy, as observed through both dark-field (DFTEM) and BFTEM after 20 dpa, is depicted in Figs. 4A and 4B, respectively.

Following a heavy-ion irradiation of 20 dpa, this binary alloy exhibited extensive nucleation of voids and black spots, as particularly evident in the BFTEM micrograph presented in Fig. 4B. It is worth emphasizing that Yi *et al.* reported an extensive chain of irradiation-induced defects to nucleate and evolve in a coarse-grained binary alloy W-5Ta (in wt.%), a terminal solid solution, at doses as low as 1.2 dpa [88]. These past results from Yi *et al.* [88] emphasize that regardless of grain-size (coarse- or ultrafine-grained) or composition (highly concentrated or terminal solid solution), WTa binary alloys suffer with radiation damage at low doses. Similarly to the irradiated UFG $W_{44}Ta_{56}$ Ta, the microstructures of both the $W_{53}Ta_{42}V_5$ and the $W_{53}Ta_{44}V_3$ RMEAs after the same 20 dpa heavy-ion irradiation are shown in Fig. 4(C,D) and 4(E,F), respectively, utilizing DFTEM and HAADF imaging. It is important to emphasize that the binary alloy as-synthesized has larger grain sizes (pertaining to the UFG regime) when compared with the ternary RMEAs, which are nanocrystalline. Instead of BFTEM imaging, HAADF was preferred to investigate the presence of voids in both ternary RMEAs as sparse voids are directly viewed as “round-black” features using this imaging mode.

While some voids were observed within the intra-granular regions of the $W_{53}Ta_{44}V_3$ RMEA (Fig. 4E), voids were not clearly detected or were not resolvable in the $W_{53}Ta_{42}V_5$ RMEA when imaged under identical conditions. It is important emphasizing that the observation of voids in both alloys is dependent on the spatial resolution of our electron-microscopes which is around 0.25 nm. In addition, the results

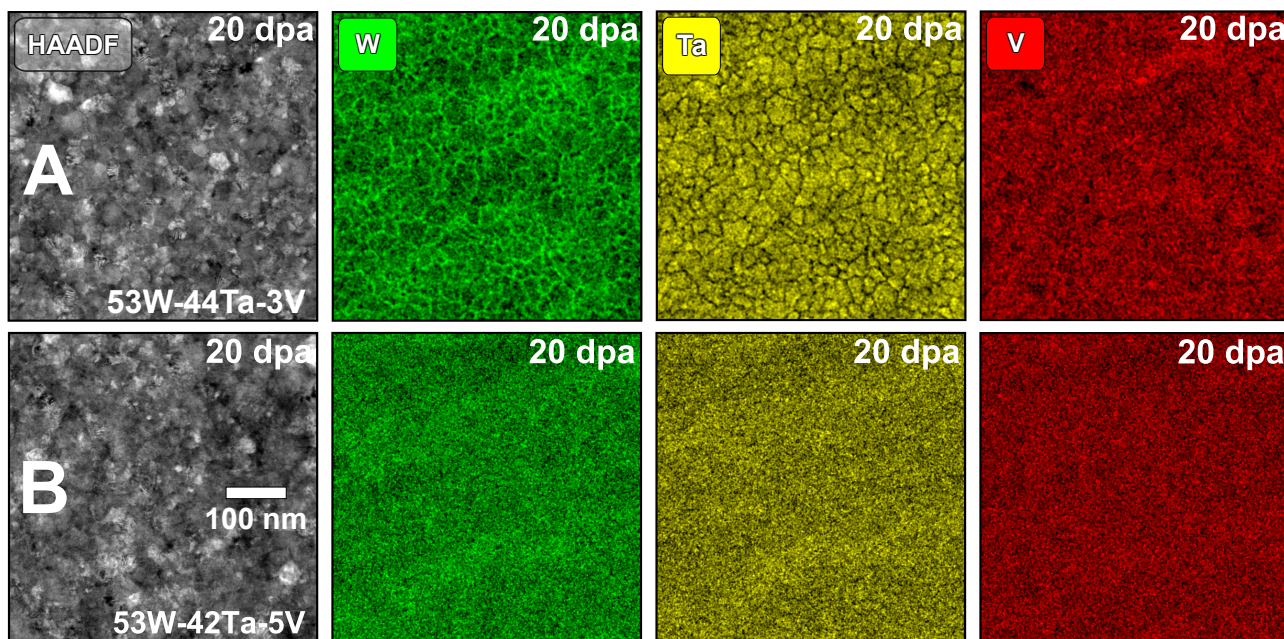


Figure 3: **Nanoscale chemistry of the WTaV RMEAs after irradiation at 20 dpa** | High-magnification STEM-EDX mapping collected from both $W_{53}Ta_{42}V_5$ (top row) and the $W_{53}Ta_{44}V_3$ (bottom row) RMEAs reveal W segregation and Ta depletion at the nanocrystalline grain boundaries upon decreasing the V content in the W–Ta–V system. The $W_{53}Ta_{42}V_5$ RMEA neither exhibit radiation-induced segregation nor radiation-induced precipitation or phase instabilities/transformations, indicating a high-radiation tolerance at 20 dpa.

indicate that nanocrystalline RMEAs exhibit superior performance compared to UFG binary alloy in terms of their resistance to the formation of black-spots and voids under irradiation, directly suggesting that the small additions of element V, increases significantly the radiation response of the binary alloy. However, it is important noting that in the specific conditions of our study, nanocrystallinity was only achieved in the W-Ta system when V was added as an alloying element. This observation underscores the potential role of V in influencing the radiation response of these new RMEAs, warranting further investigation.

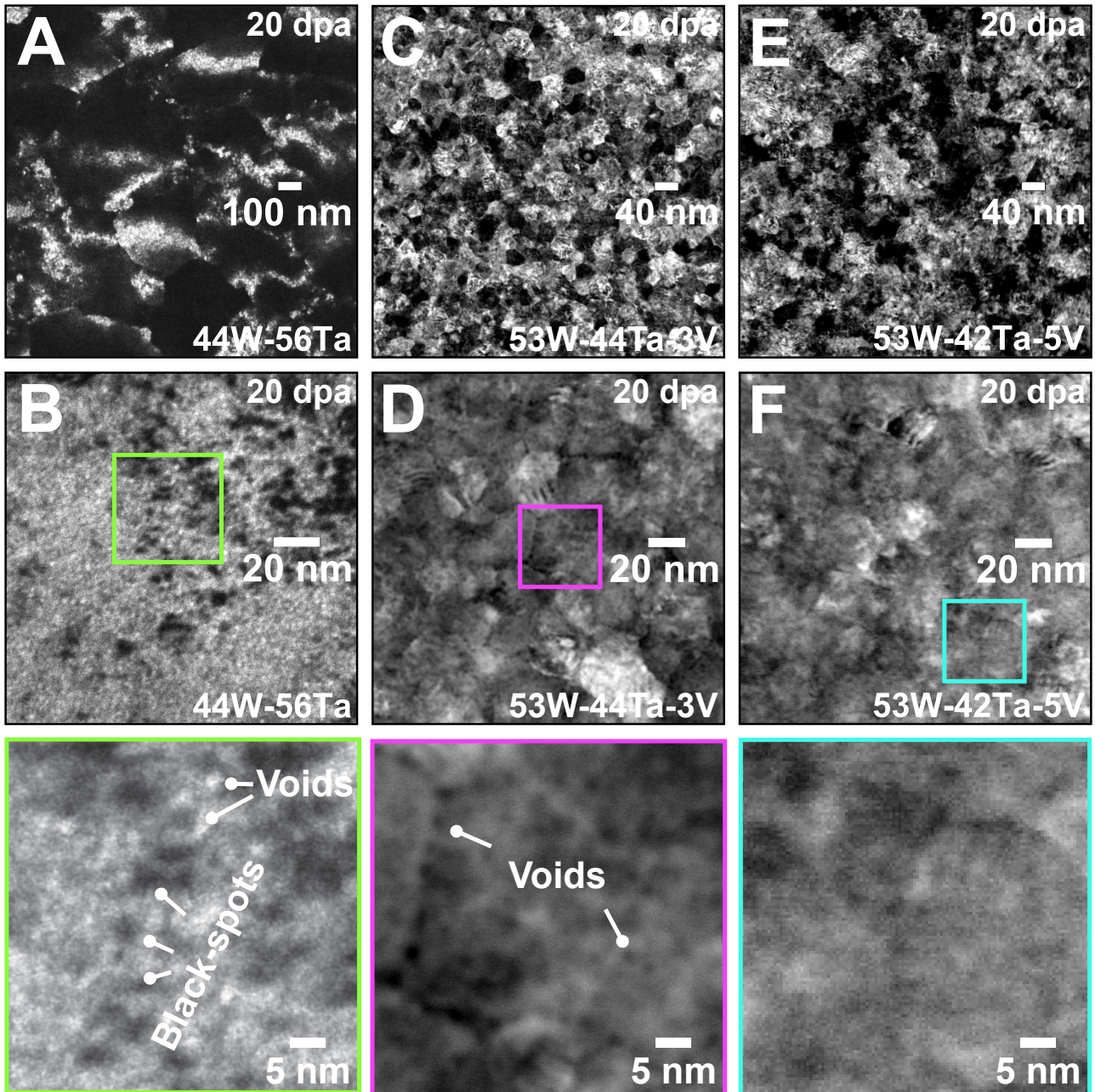


Figure 4: **Comparison between WTa and WTaV RMEAs at 20 dpa** | Grain stability and defects after irradiation are observed in the UFG $W_{44}Ta_{56}$ Ta alloy as shown in the DFTEM micrograph in **A** and the underfocused BFTEM micrograph in **B**: this binary alloy exhibit both voids and black-spots as particularly shown in **B** and its green-square inset. Grain morphology for both irradiated $W_{53}Ta_{44}V_3$ and $W_{53}Ta_{42}V_5$ RMEAs are shown in the DFTEM micrographs in **C** and **E**: both alloys' microstructures are stable in terms of grain-size after 20 dpa. HAADF was used to better resolve voids in the RMEAs as shown in micrographs **D** and **F**, but voids were clearly resolvable in the $W_{53}Ta_{44}V_3$ RMEA, particularly noted in its pink-square inset, whereas in the $W_{53}Ta_{42}V_5$ RMEAs, voids were barely resolvable, particularly noted in its cyan-square inset. Note: Image in **B** is a under-focused BFTEM micrograph where voids appear "round and white", whereas micrographs **D** and **F** are HAADF where voids appear "round-black".

A quantification of both voids and areal density of voids is presented in Table 2. Based on our observations of the studied alloys irradiated to 20 dpa, the $W_{53}Ta_{44}V_3$ RMEA exhibits the smaller average void sizes and areal density than the binary UFG $W_{44}Ta_{56}$ alloy: already an indicative of higher radiation tolerance for the ternary alloy with V when compared with the binary alloy. However, the most interesting observation arising from this work is that upon increasing the V content from 3 to 5 at.%, voids were not observed in the $W_{53}Ta_{42}V_5$ RMEA. The radiation tolerance of these new RMEAs is better evaluated when recent data on *in situ* TEM ion irradiation of relevant fusion materials is taken into consideration. Under similar irradiation temperatures and doses to this present work, *in situ* TEM with He implantation revealed He bubbles with an average diameter of 6.6 nm and an areal density of 2.7×10^{-2} bubbles·nm⁻² for bulk W [89, 90]. For UFG W, the average diameter of bubbles was reported to be 6.4 nm with an areal density of 7.5×10^{-2} bubbles·nm⁻² [91]. The previous $W_{38}Ta_{36}Cr_{15}V_{11}$ RHEA exhibited He bubbles of around 2.2 nm in diameter with an areal density of 1.5×10^{-1} bubbles·nm⁻² [3]. Both average void size and areal density for the $W_{53}Ta_{44}V_3$ RMEA investigated in this work are smaller than He bubbles in bulk W [89, 90], UFG W [91] and previous chemically-complex quaternary RHEAs [3], together with the fact that the $W_{53}Ta_{42}V_5$ RMEA exhibited no detectable voids. The results in this work are emphasising the new potential of such RMEAs within the ternary system of W–Ta–V present to be considered candidate fusion materials.

2.4. Chemical short-range order within the W–Ta–V system

To gain a deeper understanding of the important role of V on radiation-induced stability in the considered RMEAs, an atomistic Monte-Carlo (AMC) modelling approach based on density functional theory (DFT) and cluster expansion Hamiltonian (CEH) methods, developed recently for multi-component system [92–95], has been employed to predict the chemical short-range order (CSRO) of the three different pairs (W-Ta, W-V and Ta-V) and thermodynamic properties of both $W_{53}Ta_{44}V_3$ and $W_{53}Ta_{42}V_5$ alloys.

In agreement with our previous investigations in quinary alloys containing W, Ta and V [94, 95], the calculated Warren-Cowley CSRO parameter of the W-Ta pair averaged over first nearest-neighbour (1NN) and second nearest-neighbour (2NN) in the BCC system is negative as a function of temperature in both $W_{53}Ta_{44}V_3$ and $W_{53}Ta_{42}V_5$ as shown in Figs. 5A and 5B, respectively. This common behaviour resulting from the dominance of chemical bonding between W and Ta atoms in the 1NN and the repulsion at the 2NN can be explained by the negative enthalpy of mixing, which has been predicted in all ranges of composition in the binary W–Ta system [96]. In particular, at the composition closer to equiatomic, the above finding is related to the existence of a B₂ phase in a simple interpretation of the binary W–Ta phase diagram [97] whereas more accurate DFT calculations predicted the stability of an orthorhombic A₆B₆ phase [96].

Table 2: Average void size (diameter) and areal densities for all samples after irradiation.

Irradiated Alloy (20 dpa at 1073 K)	Average Void Size [nm]	Average Areal Density [#·nm ⁻²]
$W_{44}Ta_{56}$	1.9 ± 0.1	$8.9 \pm 0.2 \times 10^{-3}$
$W_{53}Ta_{44}V_3$	1.7 ± 0.1	$7.0 \pm 1.1 \times 10^{-3}$
$W_{53}Ta_{42}V_5$	Not observed/detected	Not observed/detected

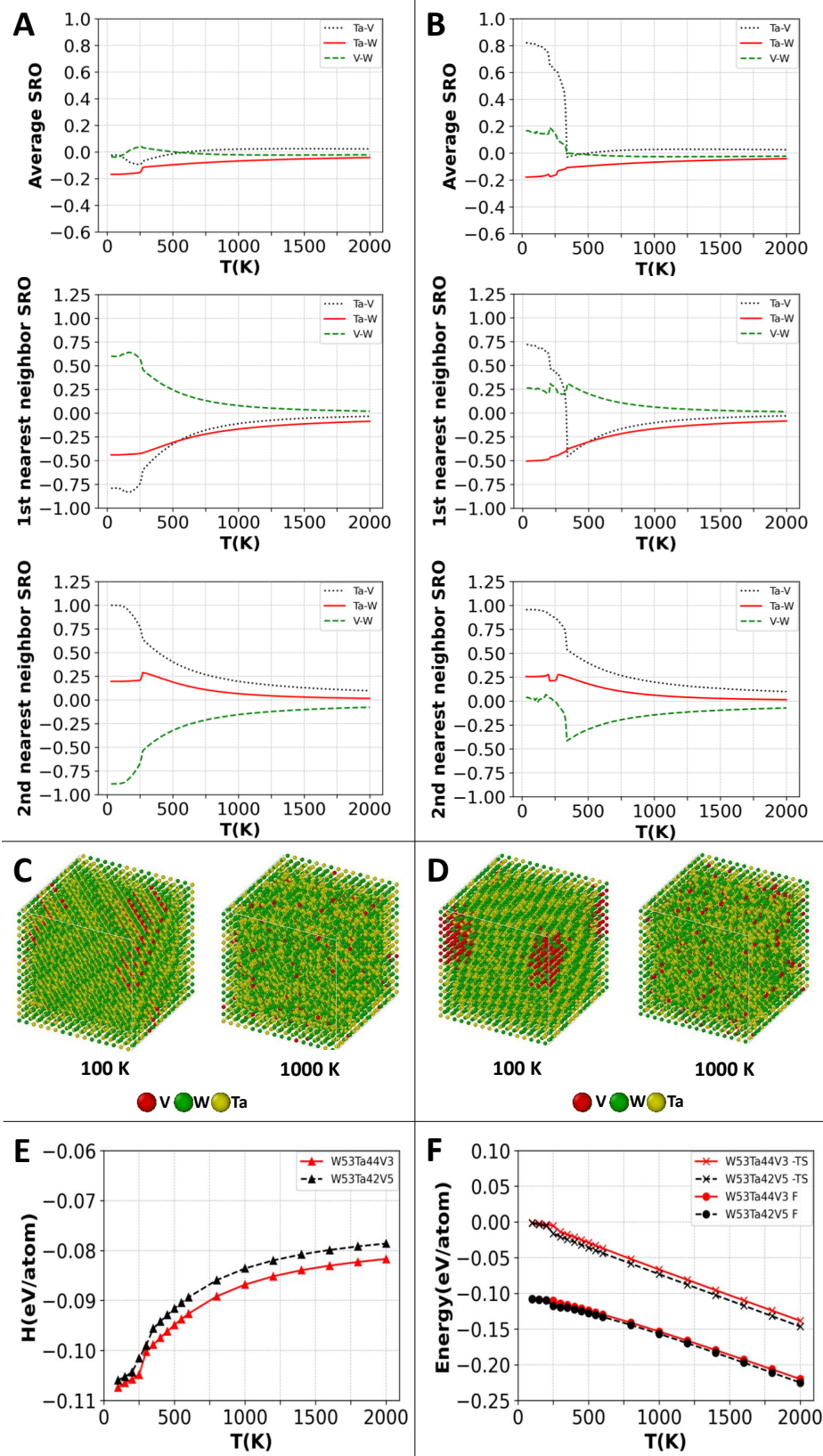


Figure 5: **DFT-CEH based AMC simulations for $W_{53}Ta_{44}V_3$ and $W_{53}Ta_{42}V_5$** | The predicted Warren-Cowley chemical short-range order parameters (average, 1NN and 2NN) for different pairs of atoms (W-Ta: blue; W-V: red and Ta-V; yellow) as a function of temperature for $W_{53}Ta_{44}V_3$ (A) and $W_{53}Ta_{42}V_5$ (B). Atomic structures obtained from AMC simulations at 100K and 1000K are shown for $W_{53}Ta_{42}V_3$ (C) and $W_{53}Ta_{44}V_5$ (D). The enthalpy of mixing (E), configuration entropy and free energy (F) calculated as a function of temperature for the two considered RMEA alloys.

The average CSRO of W-V pair in the two ternary alloys with rich W and Ta concentration is, however, quite different to those of W-Ta as depicted in Figs. 5A and 5B although a similar trend of negative enthalpy of mixing has also predicted in the binary W-V system [96]. Due to low V concentration, the CSRO W-V pair is found to be strongly positive for the 1NN, while it is mostly negative for the 2NN as a function of temperature. There is, however, a significant difference between the two alloys with different V concentrations. Namely, at low temperatures ($T < 250\text{K}$), the 2NN CSRO between W-V changes from negative to positive for the $\text{W}_{53}\text{Ta}_{42}\text{V}_5$ RMEA, whereas it continues to be negative for the $\text{W}_{53}\text{Ta}_{44}\text{V}_3$ RMEA. This means that for the latter case, V atoms are strongly to be present in the 2NN shell of a W atom, while in the former case they tend to remain far from W.

In a consistency with the above analysis for the 2NN CSRO of W-V, the second interesting difference between the two alloys considered $\text{W}_{53}\text{Ta}_{42}\text{V}_5$ and $\text{W}_{53}\text{Ta}_{44}\text{V}_3$ is found in the 1NN CSRO of Ta-V pairs. As both Ta and V are transition metals in group 5 of the periodic table, the enthalpy of mixing is expected to be positive in the binary Ta-V system and accordingly the 1NN CSRO should be positive indicating the segregation tendency between Ta and V. In a strong variance with the binary alloy system, the CSRO of the 1NN Ta-V pair in the $\text{W}_{53}\text{Ta}_{44}\text{V}_3$ RMEA is negative for all temperatures demonstrating the important effect of W concentration on the chemical SRO between Ta and V. In the $\text{W}_{53}\text{Ta}_{42}\text{V}_5$ RMEA, a similar negative trend for the 1NN CSRO of Ta-V pair is observed for temperatures higher than about 350 K, but it becomes positive for $T < 350\text{K}$. This dramatic change results in different behavior of the average CSRO parameter for Ta-V of $\text{W}_{53}\text{Ta}_{42}\text{V}_5$ in comparison with those of $\text{W}_{53}\text{Ta}_{44}\text{V}_3$ at low temperature. It is worth mentioning that our comparison of the predicted CSRO at low-temperature for the 1NN Ta-V pairs and those of the 2NN for W-V pairs in the two considered RMEAs serves as a crucial precursor to differentiate their properties systematically as a function of temperatures including the at high temperatures. For instance, at $T = 1200\text{K}$, our calculated CSRO for 1NN Ta-V and 2NN W-V are found to be -0.0803 ± 0.0005 and -0.1283 ± 0.0005 , respectively, in $\text{W}_{53}\text{Ta}_{44}\text{V}_3$ that are stronger negative than the corresponding values of -0.0736 ± 0.0006 and -0.1194 ± 0.0003 , respectively, found in the RMEA with higher V, *i.e.*, the $\text{W}_{53}\text{Ta}_{42}\text{V}_5$. Stronger negative CSRO at higher temperatures (and irradiation as it enhances solid-state diffusion) suggest a tendency for the RMEA to exhibit segregation as observed in the $\text{W}_{53}\text{Ta}_{44}\text{V}_3$ RMEA (see Fig. 3B). This segregation is suppressed upon minor additions of V to compose the $\text{W}_{53}\text{Ta}_{42}\text{V}_5$ RMEA, which has a decreased CSRO effect, resulting in increasing the chemical stability of the random solid solution.

The above analysis of CSRO parameters demonstrates a sensitivity of microstructural stability with respect to the CSRO as a function of both V concentration and temperature in the W-Ta-V system. Figures 5C and 5D show the results of AMC simulations in a cell with 16,000 atoms obtained at 100K and 1000K for $\text{W}_{53}\text{Ta}_{44}\text{V}_3$ and $\text{W}_{53}\text{Ta}_{42}\text{V}_5$ RMEAs, respectively. A stronger tendency of ordering surrounding V atoms for the former system was in good agreement with the SAED indexing in $\text{W}_{53}\text{Ta}_{44}\text{V}_3$ after irradiation (see Fig. 2F). It is worth emphasising that at high temperatures, the 1NN contribution to the CSRO behaviour for V-Ta pair is dominantly negative and much stronger for $\text{W}_{53}\text{Ta}_{44}\text{V}_3$ than those of $\text{W}_{53}\text{Ta}_{42}\text{V}_5$ as it can be seen from 5A and 5B. Our AMC simulations also indicate the more homogeneous atomic distribution in $\text{W}_{53}\text{Ta}_{42}\text{V}_5$, where there are no observations of radiation induced defects (voids) at 20 dpa at high temperature as shown in Table. 2. Finally, our calculations of enthalpy of mixing (Figs

5E), configurational entropy and free energy depicted in Figs 5F showed a more negative enthalpy of mixing for $W_{53}Ta_{44}V_3$ over $W_{53}Ta_{42}V_5$ over all the temperature range mainly due to V-driven chemical ordering effect in the former RMEA.

It is important to establish the correlation between V-Ta CSRO with the observed microstructural changes after irradiation for the two W-Ta-V RMEAs with respect to a small variation of V concentration from our AMC simulations. The lower-V alloy $W_{53}Ta_{44}V_3$ has the radiation-induced second V-bcc phase due to anomalous negative average CSRO parameter between V-Ta while the higher-V alloy $W_{53}Ta_{42}V_5$ has a dominant single W-bcc phase with a segregation tendency between V and Ta associated with the positive average CSRO. It is worth emphasizing the important role of V on distinct and low radiation-induced defect formation properties in comparison with those of W and Ta [98, 99] and therefore providing insight into enhanced radiation resistance in the bcc MEAs W-Ta-V system. Crucially, the prediction of strong change for Ta-V CSRO properties between $W_{53}Ta_{44}V_3$ and $W_{53}Ta_{42}V_5$ provides an excellent support to the experimental observation of a systematic suppression of voids from the binary $W_{44}Ta_{56}$ to the RMEAs as it is shown in Table 2. According to molecular dynamic (MD) simulations, a slow self-interstitial atom (SIA) and fast vacancy diffusion due to weak binding energies of V dumbbells in comparison with significantly larger ones of W and Ta lead to the closer mobilities of vacancies and SIAs, which enhances defect recombination in the annealing process in W-Ta-V alloys [100]. To support these findings, additional AMC simulations have been performed for $W_{44}Ta_{56}$ with 0.5% vacancy using the DFT-CEH, as reported elsewhere [92]. A strong presence of voids for this binary system is observed and in good agreement with the experimental observation shown in Fig. 4D for $W_{44}Ta_{56}$ (see Fig. S1 from Supplementary Information). Importantly, the average void size obtained from AMC simulations equal to 1.5 ± 0.4 nm agrees with the value from the experiment reported in Table 2. A further systematic investigation will be focusing on the defect properties as a function of V alloying concentration in radiation-induced microstructure stability of W-Ta-V system. Finally, it is interesting to predict new candidate MEAs with enhancing radiation resistance from a CSRO behaviour similar to those of W-Ta-V RMEAs investigated in this work. One of the candidates would be W-Ti-V alloys for which our AMC simulations were performed based on CEH developed in [94]. It is found that for $W_{53}Ti_{42}V_5$ the temperature dependence of CSRO between Ti-V as well as the enthalpy of mixing are similar to those of Ta-V at the temperature around 250K for $W_{53}Ta_{42}V_5$ leading to a potentially single bcc-based W phase at high-temperature region (See Fig. S2 from Supplementary Information).

3. Conclusions

We have demonstrated by means of irradiation-testing and characterization experiments that new RMEAs can be developed and their radiation response can be tailored as a function of minor modifications in the alloys' chemistry. Two new nanocrystalline RMEAs were synthesized and investigated in this work: $W_{53}Ta_{42}V_5$ and $W_{53}Ta_{44}V_3$. Atomistic simulations of short-range order in these bcc RMEAs unravelled the significant role of V alloying effects on radiation-induced micro-structural stability and defect formation properties in W-Ta-V via a systematic investigation of dependence in CSRO for the Ta-V in 1NN and those for the W-V in 2NN as a function of V concentration and temperature. Minor variations in V content lead to differences in phase stability and segregation behavior that were experimentally observed and

computationally validated. The transition from RHEAs to RMEAs has the potential to greatly influence the quest for materials with high radiation tolerance for the practical application in future nuclear fusion reactors. In addition, the WTaV RMEAs studied in this work address the concerns of materials' activation whilst under in-service in a fusion reactor: they both present reduced activation when comparing with existing RHEAs so far investigated. This potential arises from the reduction in chemical complexity, achieved by decreasing the number of alloying elements without jeopardizing the high-stability inherent to HEAs with four or more constituents. This simplification is aimed at facilitating the metallurgical processes for synthesizing these alloys in bulk and at larger scales, which is a necessary step for achieving both technological readiness and commercialisation of materials for future fusion reactors. Therefore, this study lays the groundwork for future investigations into defect properties as a function of V alloying concentration and the exploration of new candidate multi-element alloys with enhanced radiation resistance and simplified-chemistry, the latter manifested by a reduction on number of alloying elements, thus deviating from the original high-entropy alloy concept [51] to a new and optimized way to think and design the future materials for nuclear fusion.

4. Materials and Methods

4.1. Synthesis of the WTa and WTaV alloys

Metallic alloys in the binary system W–Ta and the ternary system W–Ta–V were prepared in a form of thin solid films using the magnetron-sputtering deposition technique from elemental targets with nominal 99.99 at.% purity. The deposition was performed at room temperature, 3 mTorr of pressure and with no bias voltage. Multiple thin solid films were deposited on pure NaCl (100) substrates from Hilger Crystals, Inc. After deposition, the substrates were dissolved in a deionized water and pure ethanol solution and the floating films were placed onto pure Mo mesh grids for TEM analysis and irradiation. The thickness of the deposited alloys was estimated to be ≈ 70 nm using profilometry. .

4.2. Heavy-ion irradiations with *in situ* TEM

All the alloys investigated in this work were irradiated with 1 MeV Kr heavy-ions with *in situ* TEM at the Intermediate Voltage Electron Microscope (IVEM) Tandem facility located at the Argonne National Laboratory. Prior irradiation, the samples were subjected to 10 min of annealing at 1173 K using a Gatan double-tilt heating holder (furnace-type). Irradiations were then carried out at temperature of 1073 K with a Kr flux measured to be 1.25×10^{12} ions \cdot cm $^{-2}$ \cdot s $^{-1}$. BFTEM micrographs and SAED patterns were recorded before and after irradiation. During irradiation, the samples were under constant electron-beam monitoring using a Hitachi TEM 9000 operating a LaB₆ filament at 300 keV. Multiple videos were recorded during both annealing and irradiation and can be found in the supplemental files. Fluence-to-dpa calculations were performed using the Stopping and Range of Ions in Matter (SRIM) Monte Carlo code version 2013 [101]. For these calculations, a procedure described by Stoller *et al.* was used [102], which consists in using the Quick-Damage calculation mode setting the displacement energies for all transition metals to 40 eV. The alloys in this study were subjected to 1 h of irradiation, achieving a fluence of 4.50×10^{15} ions \cdot cm $^{-2}$, equivalent to an average of 20 dpa across the assumed 100 nm sample thicknesses and the SRIM calculated default densities (in g \cdot cm $^{-3}$). A plot of dose in dpa as a function of the irradiation depth is shown in the supplemental information file.

4.3. Post-irradiation screening with conventional and analytical S/TEM

Following irradiation, the samples were allowed to cool within the TEM's vacuum environment by deactivating the external heating supply provided by GATAN. After cooling, these samples were removed for further post-irradiation carried out at a FEI Titan 80-300 STEM located at the Los Alamos National Laboratory and also using a Thermo Fisher Talos F200X located at the Montanuniversität Leoben. Post-irradiation characterisation was performed using STEM mode and the High-Angle Annular Dark-Field (HAADF) and Bright-Field (BF) detectors as well as Energy Dispersive X-ray (EDX) spectroscopy that was used for elemental mapping of the unirradiated and irradiated alloys. Dark-Field TEM (DFTEM) was also used. Selected-Area Electron Diffraction (SAED) was used to assess the phase stability of the alloys in pristine condition as well as after annealing at 1173 K and after irradiation at 1073 K. SAED pattern indexing was performed with data available in the ICSD database [86], more specifically: ICSD-52268 for W (BCC) [84], ICSD-53786 for Hf (HCP) [85], and ICSD-171003 for V (BCC) [87].

4.4. Modelling and calculation techniques

In this study, Atomistic Monte Carlo (AMC) simulations were performed using Cluster Expansion Hamiltonian (CEH) formalism which has been recently developed for studying the phase stability of compositionally complex and multi-component systems as a function of temperature and irradiation damage for different structural materials based on W-based [92, 94–96, 103] and Fe-based [104, 105] alloys. The CEH can be written in the following formula [92]:

$$\Delta H_{mix}^{CEH}(\vec{\sigma}) = \sum_{\omega, n, s} J_{\omega, n}^{(s)} m_{\omega, n}^{(s)} \langle \Gamma_{\omega', n'}^{(s')}(\vec{\sigma}) \rangle_{\omega, n, s}, \quad (1)$$

where the summation is performed over all the clusters, distinct under symmetry operations in the BCC lattice for the present study. $\vec{\sigma}$ denotes the ensemble of occupation variables in the lattice. ω and n are the cluster size and its shell label, respectively. $m_{\omega, n}^{(s)}$ denotes the site multiplicity of the decorated clusters (in per-lattice-site units); and $J_{\omega, n}^{(s)}$ represents the many-body effective cluster interaction (ECI) energy corresponding to the same (s) decorated cluster. In Eq.(1), $\langle \Gamma_{\omega', n'}^{(s')}(\vec{\sigma}) \rangle_{\omega, n, s}$ denotes the cluster function, averaged over all the clusters of size, ω' , and label, n' , decorated by the sequence of point functions, (s'). Within the matrix formulation of CEH for a system with K elements, the cluster function is related to the probability function of finding cluster via the formula [93]:

$$y_{\omega, n}^{(AB\dots)} = \overbrace{(\bar{\tau}_K^{-1} \otimes \dots \otimes \bar{\tau}_K^{-1})_{AB\dots, ij\dots}}^{\omega} \langle \Gamma_{\omega, n}^{(ij\dots)} \rangle \quad (2)$$

where the matrix elements of the inverse of the $(\bar{\tau}_K)$ matrix are defined by the expression [93]:

$$(\bar{\tau}_K^{-1})_{ij} = \begin{cases} \frac{1}{K} & \text{if } j = 0, \\ -\frac{2}{K} \cos\left(2\pi \left[\frac{j}{2}\right] \frac{\sigma_i}{K}\right) & \text{if } j > 0 \text{ and } j-1 < K \text{ and } j \text{ odd,} \\ -\frac{2}{K} \sin\left(2\pi \left[\frac{j}{2}\right] \frac{\sigma_i}{K}\right) & \text{if } j > 0 \text{ and } j \text{ even,} \\ -\frac{1}{K} \cos\left(2\pi \left[\frac{j}{2}\right] \frac{\sigma_i}{K}\right) & \text{if } j-1 = K \text{ and } j \text{ odd.} \end{cases} \quad (3)$$

and $i, j = 0, 1, 2, \dots, (K-1)$, j and $\lceil \frac{j}{2} \rceil$ stands for the ceiling function - rounding up to the closest integer. From the Eq.(2), the point probability function is written as:

$$y_{1,1}^A = \sum_s (\bar{\tau}_K^{-1})_{A,(s)} \langle \Gamma_{1,1}^{(s)} \rangle, \quad (4)$$

and the pair probability function is determined by the following formula :

$$y_{2,n}^{AB} = \sum_s (\bar{\tau}_K^{-1} \otimes \bar{\tau}_K^{-1})_{A,B,(s)} \langle \Gamma_{2,n}^{(s)} \rangle. \quad (5)$$

Eq.(5) allows the two-body cluster probability to be linked with the Warren-Cowley short-range order (SRO) parameter, $\alpha_{2,n}^{(AB)}$, via the definition [106, 107]:

$$y_{2,n}^{AB} = x_A x_B (1 - \alpha_{2,n}^{AB}) \quad (6)$$

where x_A and x_B denote the bulk concentration of the chemical species A and B, respectively. In the case where $\alpha_{2,n}^{AB} = 0$, the pair probability is given by the product of their concentrations $x_A x_B$ corresponding to random configuration of A and B species in an alloy system. In the case of $\alpha_{2,n}^{AB} > 0$, clustering or segregation between A-A and B-B pairs is favoured and for $\alpha_{2,n}^{AB} < 0$, the chemical ordering of A-B pairs occurs. By combining Eqs.(4),(5 and (6), the SRO parameters for K -component system can be calculated by the general expression as follows [92]:

$$\alpha_{2,n}^{AB} = 1 - \frac{\sum_s (\bar{\tau}_K^{-1} \otimes \bar{\tau}_K^{-1})_{A,B,(s)} \langle \Gamma_{2,n}^{(s)} \rangle}{(\sum_s (\bar{\tau}_K^{-1})_{A,(s)} \langle \Gamma_{1,1}^{(s)} \rangle) (\sum_s (\bar{\tau}_K^{-1})_{B,(s)} \langle \Gamma_{1,1}^{(s)} \rangle)}. \quad (7)$$

The expression to calculate the average SRO parameter for first and second nearest neighbours in a BCC lattice is given by [108]:

$$\alpha_{avg}^{AB} = \frac{8\alpha_{2,1}^{AB} + 6\alpha_{2,2}^{AB}}{14} \quad (8)$$

where $\alpha_{2,1}^{AB}$ and $\alpha_{2,2}^{AB}$ are the first and second nearest neighbours SRO parameters, respectively.

The CEH, defined by Eq. (1) can be used to explicitly determine the configuration entropy of a K -component system via the thermodynamic integration method [104, 105]. Here the entropy is computed from fluctuations of the enthalpy of mixing at a given temperature using the following formula

$$S_{conf}[T] = \int_0^T \frac{C_{conf}(T')}{T'} dT' = \int_0^T \frac{\langle [\Delta H_{mix}^{CEH}(T')]^2 \rangle - \langle \Delta H_{mix}^{CEH}(T') \rangle^2}{T'^3} dT', \quad (9)$$

where $\langle [\Delta H_{mix}^{CEH}(T')]^2 \rangle$ and $\langle \Delta H_{mix}^{CEH}(T') \rangle^2$ are the square of the mean and mean square enthalpies of mixing, respectively. The statistical average over configurations at finite temperature in Eq.(9) can be performed by combining the CEH with atomistic Monte Carlo (AMC) technique.

The CEH is constructed by mapping a large database of Density Functional Theory (DFT) energies of not only randomized solution structures but also for intermetallic ordered structures with the different

compositions [92, 94–96]. Within the present study for W–Ta–V alloys, the set of ECIs energies obtained from our recent study [95] have been employed as it takes into consideration not only two and three but also four-body cluster interaction which is crucial in discovering the important role of the CSRO V-Ta CSRO parameter. In this work, semi-canonical exchange AMC simulations were performed using Alloy Theoretic Automated toolkit (ATAT) [109, 110] package for the BCC $20 \times 20 \times 20$ super-cell with 16000 atoms. For each composition of the ternary W–Ta–V alloys, the simulation computes the enthalpy of mixing at each temperature step for reaching a thermodynamic equilibrium configuration. The start temperature for each simulation begins at 2000 K and is reduced to 10 K with temperature steps of 10 K. The start temperature is chosen such that a disordered configuration is near-guaranteed after 2000 MC steps per atom in the thermalization and accumulation stages. The free energy of an alloy at each temperature is calculated from the enthalpy of mixing and the configuration entropy determined by Eq.(9). The error bars of CSRO parameters can be determined by Eq.(7) using AMC simulations of average cluster functions calculated from thermodynamic equilibrium configurations generated for each temperature and alloy composition.

Acknowledgements

Research presented in this article was supported by the Laboratory Directed Research and Development (LDRD) program of Los Alamos National Laboratory primarily under project number 20220597ECR. MAT acknowledges support from the LDRD program 20200689PRD2. This work was performed, in part, at the Center for Integrated Nanotechnologies, an Office of Science User Facility operated for the U.S. Department of Energy (DOE) Office of Science. Los Alamos National Laboratory, an affirmative action equal opportunity employer, is managed by Triad National Security, LLC for the U.S. Department of Energy NNSA, under contract 89233218CNA000001. DNM, JSW and DS work has been carried out within the framework of the EUROfusion Consortium, funded by the European Union via the Euratom Research and Training Programme (Grant Agreement No 101052200 - EUROfusion). The work at UKAEA was partially supported by the Broader Approach Phase II agreement under the PA of IFERC2-T2PA02. Views and opinions expressed are however those of the author(s) only and do not necessarily reflect those of the European Union or the European Commission. Neither the European Union nor the European Commission can be held responsible for them. DNM also acknowledges funding by the EPSRC Energy Programme [grant number EP/W006839/1]. The work at WUT has been carried out as a part of an international project co-financed from the funds of the program of the Polish Minister of Science and Higher Education through the PMW program in 2023. DNM and JSW would like to thank the support from high-performing computing facility MARCONI (Bologna, Italy) provided by EUROfusion. All the authors are grateful for funding provided by the Austrian Research Promotion Agency (FFG) in the project 3DnanoAnalytics (FFG-No 858040).

CRedit author statement

- Conceptualization and Visualization:
- Methodology, Investigation, Data Curation, Formal Analysis:
- Resources:

- Supervision and Funding Acquisition:
- Writing Original Draft: .
- Writing Review and Editing: All authors.
- Project administration: .

Data availability

The raw data required to reproduce these findings are available in the Mendeley Data permanent repository: [10.17632/y326fsd8ww.1](https://doi.org/10.17632/y326fsd8ww.1).

References

- [1] Zinkle, S. J. Fusion materials science: Overview of challenges and recent progress. *Physics of Plasmas* **12** (2005).
- [2] Zinkle, S. J. Challenges in developing materials for fusion technology-past, present and future. *Fusion Science and Technology* **64**, 65–75 (2013).
- [3] El-Atwani, O. *et al.* Outstanding radiation resistance of tungsten-based high-entropy alloys. *Science advances* **5**, eaav2002 (2019).
- [4] El Atwani, O. *et al.* A quinary WTaCrVHf nanocrystalline refractory high-entropy alloy withholding extreme irradiation environments. *nature communications* **14**, 2516 (2023).
- [5] El-Atwani, O. *et al.* In-situ TEM observation of the response of ultrafine-and nanocrystalline-grained tungsten to extreme irradiation environments. *Scientific reports* **4**, 4716 (2014).
- [6] El-Atwani, O. *et al.* Ultrafine tungsten as a plasma-facing component in fusion devices: effect of high flux, high fluence low energy helium irradiation. *Nuclear Fusion* **54**, 083013 (2014).
- [7] El-Atwani, O. *et al.* The role of grain size in he bubble formation: Implications for swelling resistance. *Journal of Nuclear Materials* **484**, 236–244 (2017).
- [8] El-Atwani, O. *et al.* Nanohardness measurements of heavy ion irradiated coarse-and nanocrystalline-grained tungsten at room and high temperature. *Journal of Nuclear Materials* **509**, 276–284 (2018).
- [9] Bloom, E., Zinkle, S. & Wiffen, F. Materials to deliver the promise of fusion power—progress and challenges. *Journal of nuclear materials* **329**, 12–19 (2004).
- [10] Zinkle, S. J. Advanced materials for fusion technology. *Fusion engineering and design* **74**, 31–40 (2005).
- [11] Duffy, D. Fusion power: a challenge for materials science. *Philosophical Transactions of the Royal Society A: Mathematical, Physical and Engineering Sciences* **368**, 3315–3328 (2010).
- [12] Knaster, J., Moeslang, A. & Muroga, T. Materials research for fusion. *Nature Physics* **12**, 424–434 (2016).
- [13] Rowcliffe, A. F., Garrison, L. M., Yamamoto, Y., Tan, L. & Kato, Y. Materials challenges for the fusion nuclear science facility. *Fusion Engineering and Design* **135**, 290–301 (2018).
- [14] Wirth, B., Nordlund, K., Whyte, D. & Xu, D. Fusion materials modeling: Challenges and opportunities. *MRS bulletin* **36**, 216–222 (2011).
- [15] Sharp, J. *et al.* Investigation of the microstructure of He⁺ ion-irradiated TiBe₁₂ and CrBe₁₂ using ex-situ transmission electron microscopy. *Journal of Nuclear Materials* **588**, 154812 (2024).
- [16] Davis, J., Barabash, V., Makhankov, A., Plöchl, L. & Slattery, K. Assessment of tungsten for use in the ITER plasma facing components. *Journal of nuclear materials* **258**, 308–312 (1998).
- [17] Neu, R. *et al.* Tungsten: an option for divertor and main chamber plasma facing components in future fusion devices. *Nuclear fusion* **45**, 209 (2005).
- [18] Rieth, M. *et al.* Tungsten as a structural divertor material. *Advances in Science and Technology* **73**, 11–21 (2011).
- [19] Wurster, S. *et al.* Recent progress in r&d on tungsten alloys for divertor structural and plasma facing materials. *Journal of Nuclear Materials* **442**, S181–S189 (2013).
- [20] Rieth, M. *et al.* Recent progress in research on tungsten materials for nuclear fusion applications in europe. *Journal of Nuclear Materials* **432**, 482–500 (2013).

- [21] Ren, C. *et al.* Methods for improving ductility of tungsten – a review. *International Journal of Refractory Metals and Hard Materials* **75**, 170–183 (2018).
- [22] Harrison, R. W., Greaves, G., Hinks, J. & Donnelly, S. Engineering self-organising helium bubble lattices in tungsten. *Scientific reports* **7**, 7724 (2017).
- [23] Harrison, R., Ebert, S., Hinks, J. & Donnelly, S. Damage microstructure evolution of helium ion irradiated SiC under fusion relevant temperatures. *Journal of the European Ceramic Society* **38**, 3718–3726 (2018).
- [24] Harrison, R. On the use of ion beams to emulate the neutron irradiation behaviour of tungsten. *Vacuum* **160**, 355–370 (2019).
- [25] Yi, X. *et al.* A study of helium bubble production in 10 keV He⁺ irradiated tungsten. *Fusion Engineering and Design* **125**, 454–457 (2017).
- [26] Yi, X. *et al.* High-temperature damage evolution in 10 keV He⁺ irradiated W and W-5Re. *Materials Characterization* **145**, 77–86 (2018).
- [27] Ferroni, F. *et al.* High temperature annealing of ion irradiated tungsten. *Acta Materialia* **90**, 380–393 (2015).
- [28] Reiser, J. *et al.* Ductilisation of tungsten (W): On the increase of strength AND room-temperature tensile ductility through cold-rolling. *International Journal of Refractory Metals and Hard Materials* **64**, 261–278 (2017).
- [29] Bonnekoh, C., Hoffmann, A. & Reiser, J. The brittle-to-ductile transition in cold rolled tungsten: On the decrease of the brittle-to-ductile transition by 600 K to 65°C. *International Journal of Refractory Metals and Hard Materials* **71**, 181–189 (2018).
- [30] Bonnekoh, C. *et al.* The brittle-to-ductile transition in cold rolled tungsten plates: impact of crystallographic texture, grain size and dislocation density on the transition temperature. *International Journal of Refractory Metals and Hard Materials* **78**, 146–163 (2019).
- [31] Bonnekoh, C. *et al.* The brittle-to-ductile transition in cold-rolled tungsten sheets: the rate-limiting mechanism of plasticity controlling the BDT in ultrafine-grained tungsten. *Journal of Materials Science* **55**, 12314–12337 (2020).
- [32] Riesch, J. *et al.* Properties of drawn W wire used as high performance fibre in tungsten fibre-reinforced tungsten composite. In *IOP Conference Series: Materials Science and Engineering*, vol. 139, 012043 (IOP Publishing, 2016).
- [33] Riesch, J. *et al.* Tensile behaviour of drawn tungsten wire used in tungsten fibre-reinforced tungsten composites. *Physica Scripta* **2017**, 014032 (2017).
- [34] Nikolić, V., Riesch, J. & Pippan, R. The effect of heat treatments on pure and potassium doped drawn tungsten wires: Part i-microstructural characterization. *Materials Science and Engineering: A* **737**, 422–433 (2018).
- [35] Nikolić, V., Riesch, J., Pfeifenberger, M. J. & Pippan, R. The effect of heat treatments on pure and potassium doped drawn tungsten wires: Part ii-fracture properties. *Materials Science and Engineering: A* **737**, 434–447 (2018).
- [36] Faleschini, M., Kiener, D., Knabl, W. & Pippan, R. Fracture toughness investigations of tungsten alloys and severe plastic deformed tungsten alloys. In *International PLANSEE Seminar*, 701–711 (2005).
- [37] Faleschini, M., Kreuzer, H., Kiener, D. & Pippan, R. Fracture toughness investigations of tungsten alloys and SPD tungsten alloys. *Journal of Nuclear Materials* **367**, 800–805 (2007).
- [38] Raabe, D. *et al.* Grain boundary segregation engineering in metallic alloys: A pathway to the design of interfaces. *Current Opinion in Solid State and Materials Science* **18**, 253–261 (2014).
- [39] Wurmschuber, M. *et al.* Enhancing mechanical properties of ultrafine-grained tungsten for fusion applications. *International Journal of Refractory Metals and Hard Materials* **111**, 106125 (2023).
- [40] Wurmschuber, M. *et al.* Small-scale fracture mechanical investigations on grain boundary doped ultrafine-grained tungsten. *Acta Materialia* **250**, 118878 (2023).
- [41] Pippan, R. & Hohenwarter, A. The importance of fracture toughness in ultrafine and nanocrystalline bulk materials. *Materials Research Letters* **4**, 127–136 (2016).
- [42] Hohenwarter, A. & Pippan, R. Fracture and fracture toughness of nanopolycrystalline metals produced by severe plastic deformation. *Philosophical Transactions of the Royal Society A: Mathematical, Physical and Engineering Sciences* **373**, 20140366 (2015).
- [43] Pineau, A., Benzerga, A. A. & Pardoën, T. Failure of metals I: Brittle and ductile fracture. *Acta Materialia* **107**, 424–483 (2016).
- [44] Pineau, A., Benzerga, A. A. & Pardoën, T. Failure of metals III: Fracture and fatigue of nanostructured metallic materials.

- Acta Materialia* **107**, 508–544 (2016).
- [45] Li, M., Kirk, M. A., Baldo, P. M. & Ryan, E. A. TEM with in situ ion irradiation of nuclear materials: The IVEM-tandem user facility. *Microscopy and Microanalysis* **21**, 437–438 (2015).
- [46] Hinks, J., Van Den Berg, J. & Donnelly, S. MIAMI: Microscope and ion accelerator for materials investigations. *Journal of Vacuum Science & Technology A* **29** (2011).
- [47] Greaves, G. *et al.* New microscope and ion accelerators for materials investigations (MIAMI-2) system at the University of Huddersfield. *Nuclear Instruments and Methods in Physics Research Section A: Accelerators, Spectrometers, Detectors and Associated Equipment* **931**, 37–43 (2019).
- [48] Yi, X. *et al.* In situ study of self-ion irradiation damage in w and w-5re at 500 c. *Philosophical Magazine* **93**, 1715–1738 (2013).
- [49] Yi, X., Jenkins, M. L., Hattar, K., Edmondson, P. D. & Roberts, S. G. Characterisation of radiation damage in w and w-based alloys from 2 mev self-ion near-bulk implantations. *Acta Materialia* **92**, 163–177 (2015).
- [50] Yi, X., Jenkins, M. L., Kirk, M. A., Zhou, Z. & Roberts, S. G. In-situ tem studies of 150 kev w+ ion irradiated w and w-alloys: Damage production and microstructural evolution. *Acta Materialia* **112**, 105–120 (2016).
- [51] Cantor, B., Kim, K. & Warren, P. J. Novel multicomponent amorphous alloys. *Journal of Metastable and Nanocrystalline Materials* **13**, 27–32 (2002).
- [52] Ranganathan, S. Alloyed pleasures: Multimetallc cocktails. *Current science* **85**, 1404–1406 (2003).
- [53] Yeh, J.-W. *et al.* Nanostructured high-entropy alloys with multiple principal elements: novel alloy design concepts and outcomes. *Advanced engineering materials* **6**, 299–303 (2004).
- [54] Cantor, B., Chang, I., Knight, P. & Vincent, A. Microstructural development in equiatomic multicomponent alloys. *Materials Science and Engineering: A* **375**, 213–218 (2004).
- [55] Miracle, D. B. & Senkov, O. N. A critical review of high entropy alloys and related concepts. *Acta Materialia* **122**, 448–511 (2017).
- [56] Senkov, O., Wilks, G., Miracle, D., Chuang, C. & Liaw, P. Refractory high-entropy alloys. *Intermetallics* **18**, 1758–1765 (2010).
- [57] Gao, M. *et al.* Design of refractory high-entropy alloys. *Jom* **67**, 2653–2669 (2015).
- [58] Senkov, O. N., Miracle, D. B., Chaput, K. J. & Couzinie, J.-P. Development and exploration of refractory high entropy alloys—a review. *Journal of materials research* **33**, 3092–3128 (2018).
- [59] Srikanth, M., Annamalai, A. R., Muthuchamy, A. & Jen, C.-P. A review of the latest developments in the field of refractory high-entropy alloys. *Crystals* **11**, 612 (2021).
- [60] Koch, C. C. Nanocrystalline high-entropy alloys. *Journal of Materials Research* **32**, 3435–3444 (2017).
- [61] Schuh, B. *et al.* Mechanical properties, microstructure and thermal stability of a nanocrystalline CoCrFeMnNi high-entropy alloy after severe plastic deformation. *Acta Materialia* **96**, 258–268 (2015).
- [62] Straumal, B. B. *et al.* Severe plastic deformation and phase transformations in high entropy alloys: A review. *Crystals* **12**, 54 (2021).
- [63] Vaidya, M., Muralikrishna, G. M. & Murty, B. S. High-entropy alloys by mechanical alloying: A review. *Journal of Materials Research* **34**, 664–686 (2019).
- [64] Braeckman, B. *et al.* High entropy alloy thin films deposited by magnetron sputtering of powder targets. *Thin Solid Films* **580**, 71–76 (2015).
- [65] Tunes, M. A., Vishnyakov, V. M. & Donnelly, S. E. Synthesis and characterisation of high-entropy alloy thin films as candidates for coating nuclear fuel cladding alloys. *Thin Solid Films* **649**, 115–120 (2018).
- [66] Zhang, Y. *et al.* Thermal stability and irradiation response of nanocrystalline CoCrCuFeNi high-entropy alloy. *Nanotechnology* **30**, 294004 (2019).
- [67] Tunes, M. A. *et al.* Irradiation stability and induced ferromagnetism in a nanocrystalline cocrcufeni highly-concentrated alloy. *Nanoscale* **13**, 20437–20450 (2021).
- [68] Tunes, M. A. *et al.* Perspectives on novel refractory amorphous high-entropy alloys in extreme environments. *Applied Materials Today* **32**, 101796 (2023).
- [69] Wei, G. *et al.* Revealing the critical role of vanadium in radiation damage of tungsten-based alloys. *Acta Materialia* 119991 (2024).

- [70] Cahn, R. W. Nanostructured materials. *Nature* **348**, 389–390 (1990).
- [71] Gleiter, H. Nanostructured materials. *Advanced Materials* **4**, 474–481 (1992).
- [72] Moriarty, P. Nanostructured materials. *Reports on Progress in Physics* **64**, 297 (2001).
- [73] Zhang, X. *et al.* Radiation damage in nanostructured materials. *Progress in Materials Science* **96**, 217–321 (2018).
- [74] Valiev, R. Z. & Langdon, T. G. Principles of equal-channel angular pressing as a processing tool for grain refinement. *Progress in materials science* **51**, 881–981 (2006).
- [75] Alexander, D. E., Was, G. S. & Rehn, L. The heat-of-mixing effect on ion-induced grain growth. *Journal of applied physics* **70**, 1252–1260 (1991).
- [76] Alexander, D. E., Was, G. S. & Rehn, L. Ion-induced grain growth in multilayer and coevaporated metal alloy thin films. *Nuclear Instruments and Methods in Physics Research Section B: Beam Interactions with Materials and Atoms* **59**, 462–466 (1991).
- [77] Alexander, D. E. & Was, G. S. Thermal-spike treatment of ion-induced grain growth: Theory and experimental comparison. *Physical Review B* **47**, 2983 (1993).
- [78] Kaoumi, D., Motta, A. & Birtcher, R. A thermal spike model of grain growth under irradiation. *Journal of Applied Physics* **104** (2008).
- [79] Brailsford, A., Bullough, R. & Hayns, M. Point defect sink strengths and void-swelling. *Journal of Nuclear Materials* **60**, 246–256 (1976).
- [80] Bullough, R., Hayns, M. & Wood, M. Sink strengths for thin film surfaces and grain boundaries. *Journal of Nuclear Materials* **90**, 44–59 (1980).
- [81] Aradi, E. *et al.* Radiation damage suppression in aisi-316 steel nanoparticles: Implications for the design of future nuclear materials. *ACS Applied Nano Materials* **3**, 9652–9662 (2020).
- [82] El-Atwani, O. *et al.* Helium implantation damage resistance in nanocrystalline W-Ta-V-Cr high entropy alloys. *Materials Today Energy* **19**, 100599 (2021).
- [83] Thornton, J. A. The microstructure of sputter-deposited coatings. *Journal of Vacuum Science & Technology A: Vacuum, Surfaces, and Films* **4**, 3059–3065 (1986).
- [84] Jette, E. R. & Foote, F. Precision determination of lattice constants. *The Journal of Chemical Physics* **3**, 605–616 (1935).
- [85] Noethling, W. & Tolksdorf, S. Die kristallstruktur des hafniums. *Zeitschrift fuer Kristallographie* **62**, 255–259 (1925).
- [86] Hellenbrandt, M. The inorganic crystal structure database (ICSD)-present and future. *Crystallography Reviews* **10**, 17–22 (2004).
- [87] Karen, P., Suard, E. & Fauth, F. Crystal structure of stoichiometric YBa₂Fe₃O₈. *Inorganic chemistry* **44**, 8170–8172 (2005).
- [88] Yi, X. *et al.* High-temperature defect recovery in self-ion irradiated w-5 wt% ta. *Nuclear Materials and Energy* **18**, 93–98 (2019).
- [89] El-Atwani, O. *et al.* Revealing the synergistic effects of sequential and simultaneous dual beam irradiations in tungsten via in-situ tem. *Journal of Nuclear Materials* **538**, 152150 (2020).
- [90] El-Atwani, O. *et al.* Temperature threshold for preferential bubble formation on grain boundaries in tungsten under in-situ helium irradiation. *Scripta Materialia* **180**, 6–10 (2020).
- [91] El Atwani, O. *et al.* In-situ helium implantation and tem investigation of radiation tolerance to helium bubble damage in equiaxed nanocrystalline tungsten and ultrafine tungsten-tic alloy. *Materials* **13**, 794 (2020).
- [92] Nguyen Manh, D. *et al.* First principles model for voids decorated by transmutation solutes: Short range order effects and application to neutron irradiated tungsten. *Physical Review Materials* **5**, 065401 (2021).
- [93] Fernandez-Caballerro, A., Fedorov, M., Wrobel, J. S., Mummery & Nguyen-Manh, D. Configurational entropy in multicomponent alloys: Matrix formulation from ab initio based hamiltonian and application to fcc Cr-Fe-Mn-Ni system. *Entropy* **21**, 68 (2019).
- [94] Sobieraj, D. *et al.* Chemical short-range order in derivative Cr-Ta-Ti-V-W high entropy alloys from first-principles thermodynamic study. *Physical Chemistry and Chemical Physics* **22**, 23929 (2020).
- [95] Alvarado, A. *et al.* Predicting short-range order evolution in W-Ta-Cr-V-Hf refractory high entropy alloys. *Scripta Materialia* **233**, 115506 (2023).
- [96] Muzyk, M., Nguyen-Manh, D., Kurzydowski, K., Baluc, N. & Dudarev, S. L. Phase stability, point defects, and elastic

- properties of W–V and W–Ta alloys. *Physical Review B* **84**, 104115 (2011).
- [97] Turchi, P. E. A., Gonis, A., Drachal, V. & Kurnovsky, J. First-principles study of stability and local order in substitutional W–Ta alloys. *Physical Review B* **64**, 085112 (2011).
- [98] Nguyen-Manh, D., Horsfield, A. P. & Dudarev, S. Self-interstitial atom defects in bcc transition metals: Group-specific trends. *Physical Review B* **73**, 020101 (2006).
- [99] Derlet, P. M., Nguyen-Manh, D. & Dudarev, S. Multiscale modeling of crowdion and vacancy defects in body-centered-cubic transition metals. *Physical Review B* **76**, 054107 (2007).
- [100] Li, Y., Yang, D. & Qiang, W. Atomistic simulations of enhanced irradiation resistance and defect properties in body-centered cubic W–V–Cr and W–Ta–V alloys. *Journal of Alloys and Compounds* **948**, 169744 (2023).
- [101] Ziegler, J. F., Ziegler, M. D. & Biersack, J. P. SRIM—The stopping and range of ions in matter (2010). *Nuclear Instruments and Methods in Physics Research Section B: Beam Interactions with Materials and Atoms* **268**, 1818–1823 (2010).
- [102] Stoller, R. E. *et al.* On the use of SRIM for computing radiation damage exposure. *Nuclear instruments and methods in physics research section B: beam interactions with materials and atoms* **310**, 75–80 (2013).
- [103] Wrobel, J. S., Nguyen-Manh, D., Kurzydowski, K. J. & Dudarev, S. L. A first-principles model for anomalous segregation in dilute ternary tungsten–rhenium–vacancy alloys. *Journal of Physics: Condensed Matter* **29**, 145403 (2017).
- [104] Wrobel, J. S. *et al.* Phase stability of ternary fcc and bcc Fe–Cr–Ni alloys. *Physical Review B* **91**, 024108 (2015).
- [105] Fedorov, M., Wrobel, J. S., Fernandez-Carabello, A., Kurzydowski, K. & Nguyen-Manh, D. Phase stability and magnetic properties in fcc Fe–Cr–Mn–Ni alloys from first-principles modeling. *Physical Review B* **101**, 174416 (2020).
- [106] Warren, B. E. *X-ray Diffraction, New York, Dover* (1990).
- [107] Cowley, J. M. Short-range order and long-range order parameters. *Physical Review* **138** (5A), 1384–1388 (1965).
- [108] Mirebeau, I. & Parette, G. Neutron study of the short range order inversion in $\text{Fe}_{1-x}\text{Cr}_x$. *Physical Review B* **82**, 104203 (2010).
- [109] van de Walle, A., Asta, M. & Ceder, G. The alloy theoretic automated toolkit: A user guide. *CALPHAD* **26**, 539–553 (2002).
- [110] van de Walle, A. & Asta, M. Self-driven lattice-model Monte Carlo simulations of alloy thermodynamic properties and phase diagrams. *Model. Simul. Mater. Sci. Eng. A* **10**, 521–538 (2002).